Magnetically recyclable Fe_3O_4/Bi_2S_3 microspheres for effective removal of Congo red dye by simultaneous adsorption and photocatalytic regeneration

Huayue Zhu [a,b,c], Ru Jiang [a,b,c,*], Jianbing Li [b,**], Yongqian Fu [a], Shengtao Jiang [a,c], Jun Yao [a,c]

[a] Zhejiang Provincial Key Laboratory of Plant Evolutionary Ecology and Conservation, Taizhou University, Taizhou, Zhejiang 318000, China
[b] Environmental Engineering Program, University of Northern British Columbia, Prince George, British Columbia V2N 4Z9, Canada
[c] Department of Environmental Engineering, Taizhou University, Taizhou, Zhejiang 318000, China

ARTICLE INFO

ABSTRACT

Novel magnetic bayberry-like Fe_3O_4/Bi_2S_3 microspheres (Fe_3O_4/Bi_2S_3 MSs) combining highly effective adsorption and photocatalytic regeneration were prepared by a facile hydrothermal method. The resultant Fe_3O_4/Bi_2S_3 MSs were characterized by XRD, SEM, EDS, VSM, BET and DRS. Fe_3O_4/Bi_2S_3 MSs possessed a relative large surface area of $36.0 \ m^2 \ g^{-1}$ and narrow pore size distribution around 4.72 nm. The equilibrium and kinetics of adsorption process followed the Langmuir isotherm model and pseudo-second-order kinetic model, respectively. Maximum adsorption capacity of CR as $92.24 \ mg \ g^{-1}$ was achieved on Fe_3O_4/Bi_2S_3 MSs, while only $66.28 \ mg \ g^{-1}$ was found on Bi_2S_3 MSs. High saturation magnetization, low coercivity and remnant magnetization values of Fe_3O_4/Bi_2S_3 MSs indicated that easy separation and fast re-dispersion in aqueous solution can be realized. What's more important, Fe_3O_4/Bi_2S_3 MSs with a stronger absorption in the visible light region can be regenerated by photocatalysis under simulated solar light irradiation. Fe_3O_4/Bi_2S_3 MSs also showed excellent stability and reusability for continuous removal of Congo red dye by synergistic adsorption and photocatalytic regeneration. As a result, Fe_3O_4/Bi_2S_3 MSs provided effective and conveniently recyclable materials for environmental remediation by means of providing the facile preparation, easy magnetic separation, high adsorption, and simple regeneration.

1. Introduction

According to the Colour Index, over 10,000 types of dyes are being manufactured, and annual worldwide dye production is more than 700,000 tons. It is estimated that about 10% of dyes used in industry are finally discharged into the aqueous environment, which is quite harmful to the human health and aquatic ecosystem due to their high carcinogenicity and toxicity [1]. For effective removal of those dyes from industrial wastewater, various techniques, including adsorption [2,3], flocculation-coagulation [4], ozonation [5], sonocatalysis [6], and photocatalysis [7–9], have been developed recently. Among those approaches, synergistic method of adsorption and photocatalysis has been shown to be an effective method to treat containing-dye wastewater [8–13].

As a direct band gap material with a gap energy (Eg) of 1.3 eV, bismuth sulfide (Bi_2S_3) has drawn intensive attention for its potential applications in photocatalysis [14–16], electrochemical applications [17–19], photodetector [20,21], environmental remediation [22–24], and solar energy conversion [25,26]. Recently, many Bi_2S_3-based nanocomposites, such as SiO_2/Bi_2S_3 [27], $BiVO_4/Bi_2S_3$ [14], Bi_2S_3/In_2S_3 [28], Bi_2S_3-BiOCl [29], CuS/Bi_2S_3 [30], Bi_2S_3/Bi_2SiO_5 [31], Bi_2S_3/g-C_3N_4 [22], and Bi_2S_3/Bi_2WO_6 [16], have been successfully fabricated by different techniques, and their novel and unique adsorption and photocatalytic properties have been extensively explored. Those studies have demonstrated that Bi_2S_3-based nanocomposites possess excellent photocatalytic performance for eliminating various toxic organic pollutants [22,23,27,28]. However, because of their small sizes, easy recovery and continuous reusility of Bi_2S_3-based nanocomposites are still a challenge in practical treatment system.

The separation and recovery of nanomaterials from solution with the use of magnetic fields is more selective, efficient and faster than centrifugation or filtration [32]. Magnetically recyclable

* Corresponding author at: No. 1139, Municipal Government Avenue, Taizhou City, Zhejiang Province 318000, China.
** Corresponding author.
E-mail addresses: jiangru0576@163.com (R. Jiang), Jianbing.Li@unbc.ca (J. Li).

materials has become an active and important field of corresponding researches [33–35]. Some magnetic chemicals have been used as the magnetic carriers, such as Fe_3O_4 [32,36–38], γ-Fe_2O_3 [9,35] and MFe_2O_4 (M = Ni, Co, Zn, Cu) [13,39], to prepare all kinds of magnetic nanocomposites. Among them, Fe_3O_4 nanoparticles with good magnetic response can accomplish the simple magnetic separation and recovery of suspended nanocomposites using an external magnet [37,40,41]. In addition, the excellent adsorption ability of Fe_3O_4 nanoparticles with high specific surface area to pollutant molecules is also conducive to effective removal of organic pollutants [42]. Recently, various types of Fe_3O_4/semiconductor nanocomposites, such as Fe_3O_4/BiOI [40], Fe_3O_4@SiO_2@BiOBr [43], ZnO–Fe_3O_4 [42,44], ZnO–Fe_3O_4@SiO_2 [45], Fe_3O_4/AgBr [46], Fe_3O_4@CuO [41], and Fe_3O_4@TiO_2 [37] have been synthesized. However, to the best of our knowledge, less research has been done on the facile synthesis and characterization of magnetically recyclable Fe_3O_4/Bi_2S_3 microspheres (Fe_3O_4/Bi_2S_3 MSs) and their application of synergistic adsorption and photocatalysis in removal of dyes under simulated solar light irradiation.

Herein, magnetic bayberry-like Fe_3O_4/Bi_2S_3 MSs were prepared using Fe_3O_4 nanoparticles as magnetic resource and Bi_2S_3 microspheres (Bi_2S_3 MSs) as main adsorbent and photocatalyst by a facile hydrothermal method. Fe_3O_4/Bi_2S_3 MSs were characterized by XRD, SEM, EDS, VSM, BET and DRS. The adsorption of magnetic bayberry-like Fe_3O_4/Bi_2S_3 MSs were evaluated via the decolorization of Congo red (abbreviated as CR, chosen as a model pollutant). Adsorption kinetics and adsorption isotherms were applied to describe the CR adsorption process on Fe_3O_4/Bi_2S_3 MSs. In addition, reusability of magnetic Fe_3O_4/Bi_2S_3 MSs were examined by simultaneous adsorption and photocatalytic regeneration under simulated solar light irradiation. This information may be useful for further application of Fe_3O_4/Bi_2S_3 MSs in removal of hazardous azo dyes from aqueous solution.

2. Materials and methods

2.1. Materials

$Bi(NO_3)_3$ $5H_2O$, $Fe(NO_3)_3$ $9H_2O$, $FeSO_4$ $7H_2O$, NH_3 H_2O (28%, v/v), thiocarbamide were purchased from Shanghai Chemical Reagents Research Institute (Shanghai, China) and used without further purification. Congo red (CR) used as model dye was purchased from Yongjia Fine Chemical Factory (Wenzhou, China).

2.2. Preparation of Fe_3O_4/Bi_2S_3 MSs

Firstly, Fe_3O_4 nanoparticles were synthesized by co-precipitation of ferric and ferrous salts under the presence of N_2 gas according to our previous literature [3]. Secondly, after 0.04 mol of thiocarbamide was dissolved completely into 50 mL of distilled water, 4 mmol of $Bi(NO_3)_3$·$5H_2O$ and 0.928 g of as-prepared Fe_3O_4 nanoparticles were added in and stirred for 30 min and the solution was then transferred to a Teflon-lined stainless steel autoclave. The autoclave was sealed and maintained at 90 °C for 12 h and then cooled down to room temperature naturally. The precipitate was collected by a permanent magnet, washed several times with deionized water and ethanol, respectively, and dried at 80 °C till constant weight. For comparison, pure Bi_2S_3 microspheres (Bi_2S_3 MSs) also were synthesized using a revised solvothermal method [47,48].

2.3. Characterization of Fe_3O_4/Bi_2S_3 MSs

X-ray powder diffraction (XRD) analysis was performed on a Bruker AXS D8-advance X-ray diffractmeter at 40 kV and 50 mA

with Cu target and Kα radiation (λ = 0.154 nm) in the range of 2θ from 10° to 70°. UV–vis diffuse reflectance spectra (UV–vis DRS) of the samples were obtained by using an UV-3100 UV–vis spectrophotometer (Hitachi Corporation, Japan). $BaSO_4$ was used as a reflectance standard in UV–vis diffuse reflectance experiment. The morphology and elemental composition of the synthesized samples were characterized by energy-dispersive X-ray spectroscopy with a scanning electron microscope (SEM, Hitachi S4800 equipped with an EDS). Nitrogen gas porosimetry measurement was obtained using a MPMS-XL-7 surface area and porosity analyzer (Quantum Design, America). VSM measurements were performed by using a MPM5-XL-5 superconducting quantum interference device (SQUID) magnetometer. The magnetization measurements were carried out in an external field up to 10 kOe at room temperature (293 K).

2.4. Evaluation of adsorption performance

Dye adsorption experiments were performed on a model KYC-1102 C thermostat shaker (Ningbo, China). Stock solutions of CR (1000 mg L^{-1}) were prepared by dissolving 1 g of CR in 1000 mL double distilled water. To carry out adsorption experiments, 0.02 g of Fe_3O_4/Bi_2S_3 MSs was added to 50 mL of CR aqueous solution with a fixed concentration under stirring at room temperature. At predetermined time intervals, about 5 mL aliquots were sampled and separated by a magnet. The remaining concentration of CR in supernatant solution was determined by using a TU 1810 UV–visible spectrophotometer (Beijing Purkinje General Instrument Co., Ltd, China). The amount of adsorption q_t (mg g^{-1}) and the decolorization efficiency η (%) can be calculated according to Eqs. (1) and (2), respectively.

$$q_t = \frac{(C_0 - C_t) \times V}{m} \tag{1}$$

$$\eta = \frac{(C_0 - C_t)}{C_t} \times 100\% \tag{2}$$

where q_t (mg g^{-1}) is the amount adsorbed per gram of adsorbent at time t (min), C_0 is the initial concentration of CR in the solution (mg L^{-1}), C_t is the instant concentration of CR at time t of adsorption (mg L^{-1}), m is the mass of the magnetic Fe_3O_4/Bi_2S_3 MSs (g), and V is the volume of solution (L).

2.5. Photocatalytic recycling under simulated solar light irradiation

The photocatalytic recycling of Fe_3O_4/Bi_2S_3 MSs was performed in a photochemical reactor (Nanjing Xujiang Electromechanical Factory, Nanjing, China) under simulated solar light irradiation. A 300 W xenon lamp was used as a simulated solar light source, which was positioned in the cylindrical quartz trap at ambient temperature controlled by a water-cooling system. In a typical experiment, 20 mg of Fe_3O_4/Bi_2S_3 MSs was dispersed into a 50 mL of CR solution (30 mg L^{-1}). Then, the dispersion was exposed to simulated solar light irradiation. During reaction, the resulting aqueous suspension containing CR and Fe_3O_4/Bi_2S_3 MSs was continuously stirred and bubbled so that the concentration of dissolved oxygen in reaction system was kept constant. At given time intervals, 5 mL of dispersion was drawn and Fe_3O_4/Bi_2S_3 MSs were separated immediately by an ordinary magnet. Residual CR concentration in supernatant was analyzed at λ_{max} = 496.0 nm using a TU 1810 UV–visible spectrophotometer (Beijing Purkinje Genaral Instrument Co., Ltd, China). Removal efficiency (η) of CR solution by Fe_3O_4/Bi_2S_3 MSs at time t can be calculated by Eq. (2).

3. Results and discussion

3.1. Characterization of materials

3.1.1. XRD analysis and UV–vis diffuse reflectance spectra

Fig. 1a represents XRD patterns of pure Fe_3O_4, Bi_2S_3 MSs and Fe_3O_4/Bi_2S_3 MSs. It can be easily found that the diffraction peaks of pure Fe_3O_4 at $2\theta = 30.32°$, $35.64°$, $43.36°$, $53.66°$, $57.26°$ and $62.87°$ match the reflections of $(2\,2\,0)$, $(3\,1\,1)$, $(4\,0\,0)$, $(4\,2\,2)$, $(5\,1\,1)$ and $(4\,4\,0)$, respectively, indexed to the cubic spinel structure of Fe_3O_4 (JCPDS 56-3107) (Fig. 1a) [44]. All of the diffraction peaks of Bi_2S_3 MSs are in good accordance with the standard card of orthorhombic Bi_2S_3 (JCPDS 75-1306) [17]. The pattern of Fe_3O_4/Bi_2S_3 MSs exhibit a coexistence of the Fe_3O_4 and Bi_2S_3, indicating the formation of the nanocomposites. No additional phases are evident found from the XRD patterns of all samples. The crystalline sizes of Fe_3O_4 and Bi_2S_3, determined by the Debye–Scherrer equation [40], were found to be 9 and 4 nm, respectively. Yavuz's research showed that 8–12 nm–size represents the optimal size for magnetic separations [32], which is further demonstrated below by VSM studies.

Fig. 1b displays the UV–vis diffuse reflectance spectra (DRS) of Fe_3O_4, Bi_2S_3 MSs and Fe_3O_4/Bi_2S_3 MSs. It is worth noting that Bi_2S_3 MSs have strong absorption over the whole visible light region [14,29]. The band gap of pure Bi_2S_3 is about 1.3 eV [22]. Pure Fe_3O_4 has photo-absorption not only in UV light range, but also in visible light range. However, light absorption of Fe_3O_4 weakens with increasing wavelength in the range of visible light. The whole light absorption ability of the Fe_3O_4/Bi_2S_3 MSs increased obviously with the introduction of Bi_2S_3, which should be attributed to the small band gap and large absorption coefficient of Bi_2S_3 [49]. Compared with the magnetic photocatalysts reported in literatures [29,43,44], Fe_3O_4/Bi_2S_3 MSs have strong absorption in the UV–visible-light region from 200 to 800 nm, implying it possible to regenerate the materials by photocatalysis under simulated solar light irradiation after Fe_3O_4/Bi_2S_3 MSs have adsorbed targeted pollutants.

3.1.2. Morphology and microstructure

The surface morphology, microstructure and sizes of Bi_2S_3 MSs and Fe_3O_4/Bi_2S_3 MSs were determined by SEM. Fig. 2a shows the low-magnification SEM image of Bi_2S_3 MSs by hydrothermal method using thiocarbamide as sulfur source. It reveals that Bi_2S_3 MSs consisted of bayberry-like microspheres with diameters in

the range of 1.3–4.5 μm [50]. The high magnified SEM image of Bi_2S_3 MSs shows that individual Bi_2S_3 microsphere was constructed with nanorods (Fig. 2b). The Bi_2S_3 nanorods grew from the center of the microsphere, resulting in the formation of a hierarchical bayberry-like Bi_2S_3 microsphere [30]. With the introduction of ferroferric oxide (Fe_3O_4), bayberry-like structure of Fe_3O_4/Bi_2S_3 MSs with an average size of 2.0 μm still could be easily obtained (Fig. 2c), and its surface is made up by thin Bi_2S_3 nanorods and Fe_3O_4 nanoparticles (Fig. 2d). It's worth noting that not all Fe_3O_4/Bi_2S_3 MSs presented perfectly spherical and their surface are more uneven than those of Bi_2S_3 MSs (Fig. 2d), indicating that the presence of Fe_3O_4 nanoparticles disturbed the growth of the Bi_2S_3 crystal to some extent. The compositions of different locations on Fe_3O_4/Bi_2S_3 MSs were determined by X-ray energy-dispersive spectroscopy (EDS), as shown in Fig. 2e and f. The EDS analysis of the surface showed peaks for Bi and S, as well for Fe and O, which reveal the implantation of the Fe_3O_4 in the Bi_2S_3 nanorods. However, there is no iron element in the interior of the microsphere, which indicated that a bayberry-like structure of Fe_3O_4/Bi_2S_3 MSs was not grown directly on the Fe_3O_4 surface.

3.1.3. Vibrating sample magnetometer

The magnetic properties of Fe_3O_4 and as-prepared Fe_3O_4/Bi_2S_3 MSs were measured and the corresponding results are shown in Fig. 3. The saturated magnetization of pure Fe_3O_4 nanoparticles was 66.50 emu g^{-1}, which is consistent with those reported in the literature [36,51]. However, the saturated magnetization of Fe_3O_4/Bi_2S_3 MSs reduced to 18.80 emu g^{-1} with the introduction of bismuth sulfide, which is still higher than the values of other reported magnetic material, such as $ZnO–Fe_3O_4@SiO_2$ [45] and Fe_3O_4/ZnO [44]. The acceptable saturation magnetization value indicated that as-prepared Fe_3O_4/Bi_2S_3 MSs were suited to easy magnetic separation. After adding an external magnetic field, complete magnetic separation of Fe_3O_4/Bi_2S_3 MSs was achieved in 30 s by a permanent magnet near the wild-mouth bottle (Fig. 3b). The coercivity and remanent magnetization values are about 13.70 Oe and 0.65 emu g^{-1} for Fe_3O_4/Bi_2S_3 MSs, respectively. The coercivity of Fe_3O_4/Bi_2S_3 MSs at room temperature is almost negligible, indicating the ferrimagnetic and superparamagnetic property of as-prepared Fe_3O_4/Bi_2S_3 MSs [51]. Once the permanent magnet was removed, the Fe_3O_4/Bi_2S_3 MSs could be easily re-dispersed in aqueous solution by a slight agitation or ultrasound, demonstrating that easy, fast separation and redispersion of the Fe_3O_4/Bi_2S_3 MSs can be realized in aqueous solution. Combined with the other unique
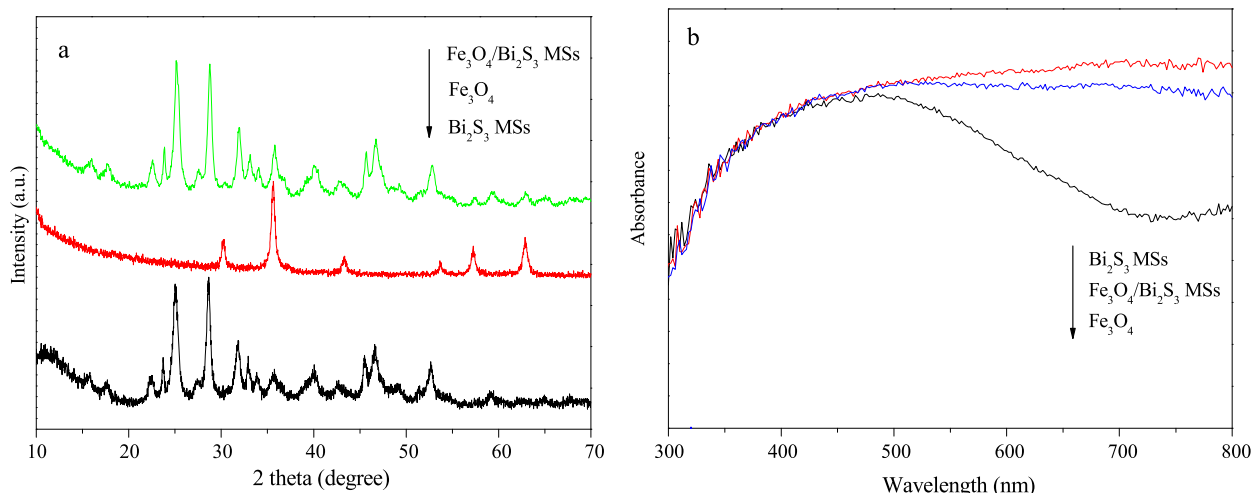

Fig. 1. XRD patterns (a) and UV–vis absorption spectra (b) of pure Fe_3O_4, Bi_2S_3 MSs, and Fe_3O_4/Bi_2S_3 MSs.

Element	Bi	S	Fe	O
Weight %	69.85	20.07	0.00	10.08
Atom%	21.02	39.36	0.00	39.62

Element	Bi	S	Fe	O
Weight %	64.04	17.39	2.59	15.97
Atom%	16.18	28.64	2.45	52.72
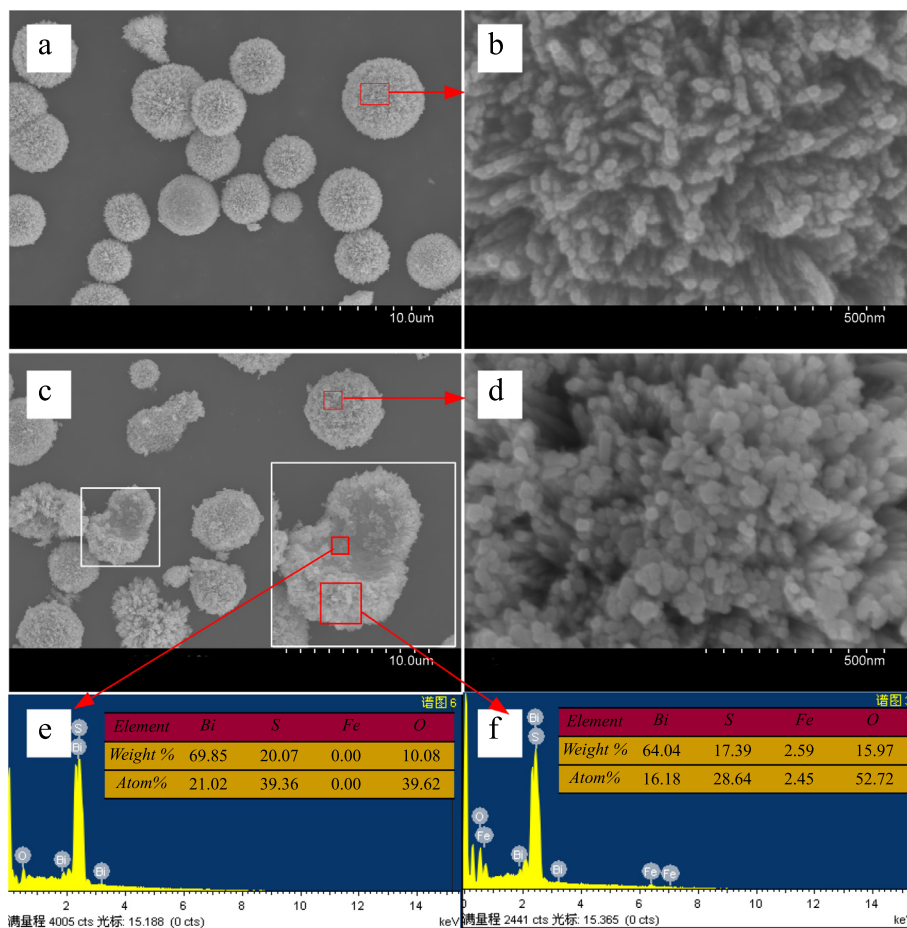
Fig. 2. SEM images of the Bi_2S_3 MSs (a, b) and magnetic Fe_3O_4/Bi_2S_3 MSs (c, d) and EDS spectrum (e, f) of Fe_3O_4/Bi_2S_3 MSs.
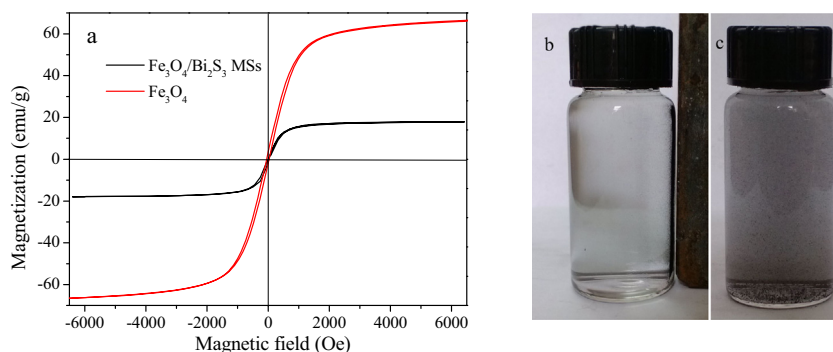
Fig. 3. Hysteresis loops curves of Fe_3O_4 and the as-prepared Fe_3O_4/Bi_2S_3 MSs(a) at 293 K (a), magnetic separation of Fe_3O_4/Bi_2S_3 MSs using an external magnet (b) and the redispersion of Fe_3O_4/Bi_2S_3 MSs (c).

properties, the magnetic Fe_3O_4/Bi_2S_3 MSs can be explored as a potential material in wastewater treatment without secondary pollution for water treatment.

3.1.4. N_2 adsorption–desorption isotherms

To give further insight into the physical structure, Brunauer-Emmet-Teller (BET) specific surface areas and the pore size distributions of Bi_2S_3 MSs and Fe_3O_4/Bi_2S_3 MSs were determined by nitrogen adsorption–desorption measurement and the results are shown in Fig. 4. As shown in Fig. 4a, the N_2 adsorption-desorption isotherm of both Bi_2S_3 MSs and Fe_3O_4/Bi_2S_3 MSs exhibit type IV, indicating the existence of abundant mesoporous

structures in those microspheres [39]. A broad hysteresis loop in the relative pressure range from 0.46 to 0.96 is reported for materials comprised of aggregates (loose assemblages) of particles forming slit like pores [52]. Compared with a BET surface area of Bi_2S_3 MSs (10.8 $m^2 g^{-1}$), the obtained Fe_3O_4/Bi_2S_3 MSs possess a relative large surface area of 36.0 $m^2 g^{-1}$. The average pore radius of Fe_3O_4/Bi_2S_3 MSs is 4.72 nm, which is less than that of the as-obtained Bi_2S_3 MSs (5.36 nm) (Fig. 5b). The high specific surface areas and mesoporous channels of magnetic Fe_3O_4/Bi_2S_3 MSs would be both favorable for improving adsorption capability and can be employed for dye-containing wastewater treatment.
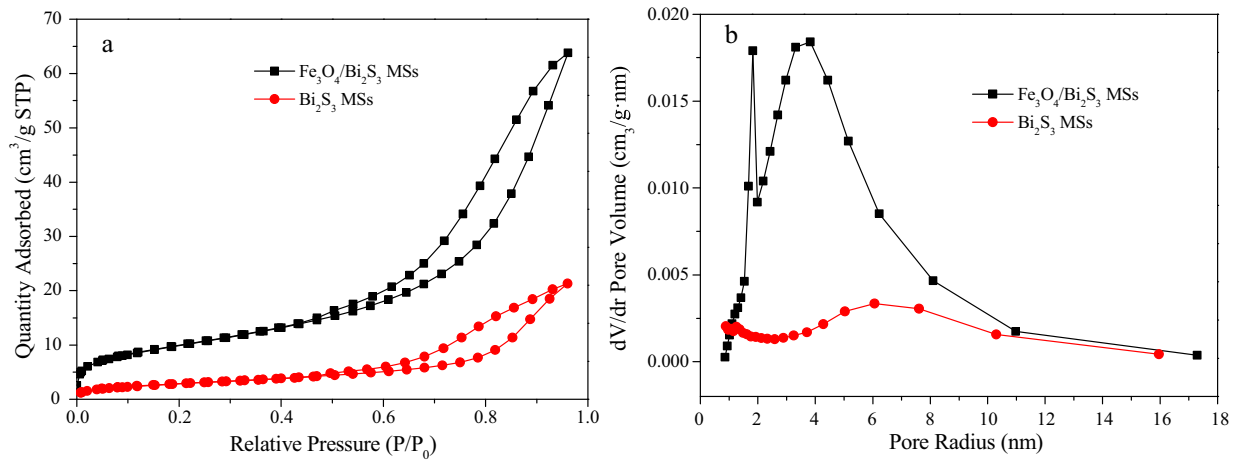
Fig. 4. Nitrogen adsorption–desorption isotherms (a) and pore-size distribution (b) of the Bi$_2$S$_3$ MSs and Fe$_3$O$_4$/Bi$_2$S$_3$ MSs.

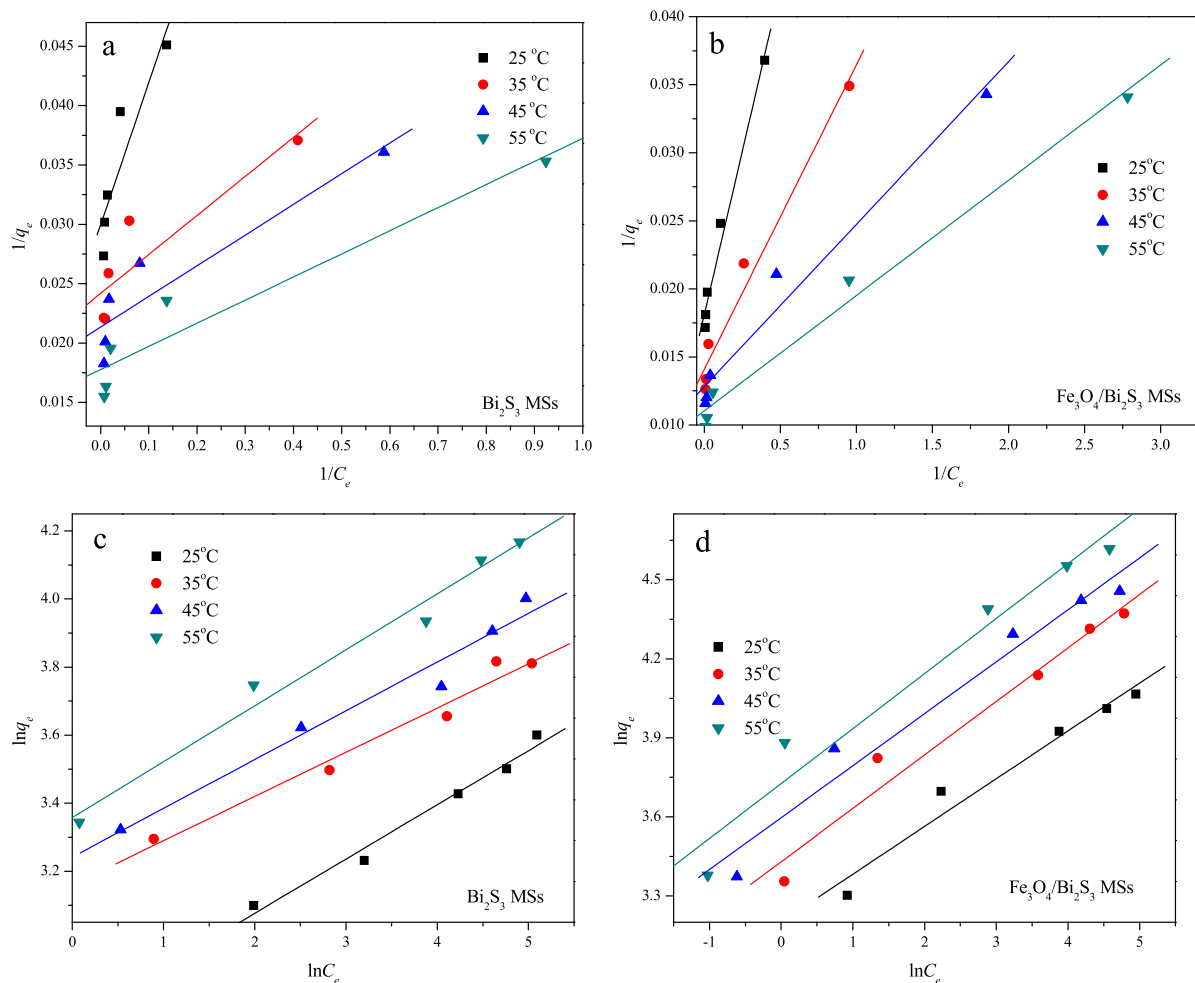**Fig. 5.** Langmuir isotherms (a, b) and Freundlich isotherms (c, d) for CR adsorption on Bi$_2$S$_3$ MSs and magnetic Fe$_3$O$_4$/Bi$_2$S$_3$ MSs.

3.2. Adsorption isotherms

Adsorption isotherm is one of important data to explain the adsorption mechanism of contaminant on novel nanocomposite [27]. In addition, the adsorption of dye on nanocomposites is an important prerequisite for a synergistic adsorption-photocatalytic degradation process [8]. Therefore, Langmuir and Freundlich isotherm models were used to analyze the equilibrium adsorption characteristics for CR dye on Bi$_2$S$_3$ MSs and Fe$_3$O$_4$/Bi$_2$S$_3$ MSs. Langmuir and Freundlich equations is represented for Eqs. (3) and (4), respectively [3].

$$\frac{c_e}{q_e} = \frac{1}{bq_m} + \frac{c_e}{q_m} \tag{3}$$

$$\ln q_e = \ln K_F + \frac{1}{n}\ln c_e \tag{4}$$

where c_e (mg L^{-1}) is equilibrium concentration of CR in solution, q_e (mg g^{-1}) is the adsorption capacity of CR adsorbed at equilibrium, q_m (mg g^{-1}) is maximum amounts of CR adsorbed per unit mass of adsorbent required for monolayer coverage of the surface, b (L mg^{-1}) is a constant related to the heat of adsorption. The slope and intercept of linear plots of c_e/q_e against c_e yield the values of $1/q_m$ and $1/bq_m$ for Eq. (3). K_F (mg$^{1-(1/n)}$ L$^{1/n}$ g^{-1}) is related to the adsorption capacity of the adsorbent and $1/n$ is another constant related to the surface heterogeneity. The slope and intercept of linear plots of $\ln q_e$ against $\ln c_e$ yield the values of $1/n$ and $\ln K_F$ for Eq. (4).

Fig. 5 shows the isotherms of CR adsorption on Bi$_2$S$_3$ MSs and Fe$_3$O$_4$/Bi$_2$S$_3$ MSs, while their maximum adsorption capacities (q_m) and some theoretical parameters (q_m, b, K_F, n, and R^2) are summarized in Table 1. It was notable that an increase in temperature resulted in a corresponding increase in adsorption capacity of CR on both Bi$_2$S$_3$ MSs and Fe$_3$O$_4$/Bi$_2$S$_3$ MSs, which showed that the adsorptions of CR onto Bi$_2$S$_3$ MSs and Fe$_3$O$_4$/Bi$_2$S$_3$ MSs are endothermic process. In general, the Langmuir isotherm model describes monolayer adsorption process while the Freundlich isotherm model describes the adsorption on heterogeneous surfaces associated with several adsorbent–adsorbate interactions [27]. For the CR adsorption on Bi$_2$S$_3$ MSs, the R^2 values ($R^2 > 0.968$) from the Freundlich equation (Eq. (4)) were all higher than those ($R^2 < 0.890$) from the Langmuir model (Eq. (3)), which is responsible for the observed multilayer adsorption. However, for the CR adsorption on Fe$_3$O$_4$/Bi$_2$S$_3$ MSs, the Langmuir equation represented the adsorption process and all R^2 values were higher than 0.972, indicating that monolayer coverage of the dye adsorbed on the surface of Fe$_3$O$_4$/Bi$_2$S$_3$ MSs. With the introduction of Fe$_3$O$_4$, magnetic Fe$_3$O$_4$/Bi$_2$S$_3$ MSs have bayberry-like structures, rough and porous surfaces and exposed more adsorption sites. As a result, the adsorption of CR on Fe$_3$O$_4$/Bi$_2$S$_3$ MSs presents monolayer adsorption process. This result is in good agreement with the observations in SEM and BET analysis of Bi$_2$S$_3$ MSs and Fe$_3$O$_4$/Bi$_2$S$_3$ MSs.

Table 2 compares the adsorption capacity of the magnetic Fe$_3$O$_4$/Bi$_2$S$_3$ MSs with the other reported inorganic adsorbents. The maximum adsorption capacity of the magnetic Fe$_3$O$_4$/Bi$_2$S$_3$ MSs towards CR is 92.24 mg g^{-1}, which is higher than those of adsorbents reported earlier, such as Fe$_{3-x}$La$_x$O$_4$ ferrite [53], Zn-Fe$_2$O$_4$ [54], Ca-bentonite [55], chitosan coated magnetic Fe$_3$O$_4$ particle [56], activated carbon [57]. It is worth mentioning that the maximum adsorption capacity (92.24 mg g^{-1}) of CR on Fe$_3$O$_4$/Bi$_2$S$_3$ MSs was almost 12.76 times higher than that of the reported activated carbon (6.7 mg g^{-1}) [57]. Therefore, Fe$_3$O$_4$/Bi$_2$S$_3$ MSs are suitable and promising for CR removal from aqueous solutions since it has a relatively high adsorption capacity and easy magnetic separation.

3.3. Effect of initial CR concentration on adsorption

Fig. 6 presents the time-dependent adsorption performance of the Bi$_2$S$_3$ MSs and magnetic Fe$_3$O$_4$/Bi$_2$S$_3$ MSs towards the removal of CR at different initial dye concentrations in aqueous solutions.

Table 2
The q_m values for the adsorption of CR on different adsorbents.

Adsorbents	q_m (mg g^{-1})	Ref.
Fe$_3$O$_4$/Bi$_2$S$_3$ MSs	92.24	This study
Chitosan coated magnetic Fe$_3$O$_4$ particle	42.62–56.66	[56]
Fe$_{3-x}$La$_x$O$_4$ ferrite	37.4–79.1	[53]
Zn-Fe$_2$O$_4$	16.58	[54]
Ca-bentonite	23.25–85.29	[55]
Activated carbon	6.7	[57]

For Bi$_2$S$_3$ MSs, as the initial concentration increased from 5 mg L^{-1} to 30 mg L^{-1}, the removal rate of CR decreased from 99% to 60% (Fig. 6a). However, the percentage of CR adsorption on Fe$_3$O$_4$/Bi$_2$S$_3$ MSs reached up to 85% within 90 min for all the studied concentrations (Fig. 6b). Compared with CR adsorption process on Bi$_2$S$_3$ MSs, the fast adsorption over the magnetic Fe$_3$O$_4$/Bi$_2$S$_3$ MSs was clearly observed for all the studied concentrations. This higher efficiency and faster rate of CR adsorption on Fe$_3$O$_4$/Bi$_2$S$_3$ MSs can be ascribed to abundant unoccupied active sites on the adsorbent's surface as well as the porous hierarchical structure of the magnetic Fe$_3$O$_4$/Bi$_2$S$_3$ MSs [3]. On the basis of the above results, the observed high adsorption capacity and the short time needed to achieve adsorption equilibrium confirm the magnetic Fe$_3$O$_4$/Bi$_2$S$_3$ MSs would be an effective adsorbent for CR removal.

3.4. Adsorption kinetics

Adsorption kinetics is one of the most important characters which govern the solute uptake rate and represent adsorption efficiency of adsorbent for design operation and optimization. To investigate adsorption kinetics of CR on Bi$_2$S$_3$ MSs and magnetic Fe$_3$O$_4$/Bi$_2$S$_3$ MSs, three different kinetic models, i.e. Lagergren-first-order model, pseudo-second-order kinetic model and intra-particle diffusion model were used to fit the adsorption kinetic data.

The Lagergren-first-order kinetic, pseudo-second-order kinetic model and intraparticle diffusion model can be given by Eqs. (5)–(7) [55].

$$\log (q_e - q_t) = \log q_e - \frac{k_1 t}{2.303} \tag{5}$$

$$\frac{t}{q_t} = \frac{1}{k_2 q_e^2} + \frac{1}{q_e} t \tag{6}$$

$$q_t = k_{id} t^{1/2} + c \tag{7}$$

where q_e and q_t (mg g^{-1}) are the amounts of CR adsorbed at equilibrium and at time t (min), respectively; k_1 is the rate constant of Lagergren-first-order kinetic model (min^{-1}). Values of k_1 can be calculated from the plots of $\log(q_e - q_t)$ versus t for Eq.(5). k_2 is the rate constant (g mg^{-1} min^{-1}) of pseudo-second-order kinetic model for adsorption. The slope and intercept of the linear plots of t/q_t against

Table 1
Adsorption isotherm constants for CR adsorption onto Bi$_2$S$_3$ MSs and magnetic Fe$_3$O$_4$/Bi$_2$S$_3$ MSs.

Adsorbent	T (°C)	$q_{e,exp}$ (mg g^{-1})	Langmuir isotherm constants			Freundlich isotherm constants		
			q_m (mg g^{-1})	b	R^2	K_F (mg$^{1-(1/n)}$ L$^{1/n}$ g^{-1})	n	R^2
Bi$_2$S$_3$ MSs	25	37.44	33.39	0.250	0.830	15.75	6.27	0.982
	35	48.48	41.36	0.736	0.813	22.81	7.69	0.972
	45	54.62	46.86	0.826	0.861	24.45	6.98	0.968
	55	66.28	56.27	0.912	0.890	26.91	6.08	0.980
Fe$_3$O$_4$/Bi$_2$S$_3$ MSs	25	53.33	55.25	0.376	0.981	23.63	5.51	0.963
	35	72.23	70.97	0.629	0.972	28.50	4.93	0.968
	45	77.24	78.064	1.073	0.973	32.45	5.07	0.962
	55	92.24	90.580	1.302	0.987	35.72	4.79	0.958

Fig. 6. CR adsorption onto Bi_2S_3 microsphere (a) and magnetic Fe_3O_4/Bi_2S_3 microsphere (b) for distinct CR initial concentrations.

t yield the values of $1/q_e$ and $1/k_2q_e^2$ for Eq. (6). c (mg g^{-1}) is the intercept and k_{id} is the intraparticle diffusion rate constant (mg g^{-1} min$^{-1/2}$), which can be calculated from the slop of the linear plots of q_t versus $t^{1/2}$.

Different kinetic parameters of CR adsorption onto Bi_2S_3 MSs and Fe_3O_4/Bi_2S_3 MSs for different CR initial concentrations were shown in Table 3. The relatively low correlation coefficient (R^2) and the large difference between the calculated value of adsorption capacity ($q_{e,cal}$) and the experimental value ($q_{e,exp}$) indicate that the adsorption kinetics of CR on the magnetic Fe_3O_4/Bi_2S_3 MSs does not obey the pseudo-first-order kinetic model. However, all the experimental data showed better compliance with pseudo-second-order kinetic model in terms of higher correlation coefficient values ($R^2 > 0.998$) and closer values between $q_{e,cal}$ and $q_{e,exp}$ (Table 3). It could be found that pseudo-second-order kinetic model was more valid to describe the adsorption behavior of CR onto Fe_3O_4/Bi_2S_3 MSs, indicating that the adsorption of CR on both Bi_2S_3 MSs and magnetic Fe_3O_4/Bi_2S_3 MSs are mainly controlled by chemisorption. Fig. 7 showed the regression plots of pseudo-second-order kinetic model about CR adsorption on both Bi_2S_3 MSs and magnetic Fe_3O_4/Bi_2S_3 MSs. It was likely that the adsorption behavior may involve valence forces by sharing of electrons between anions and bioadsorbent.

3.5. Photocatalytically recycling under simulated solar light

In addition to efficiency, the lifetime of water-treatment materials is also very important for practical applications. The reuse ability can be realized if Fe_3O_4/Bi_2S_3 MSs can self-clean CR dye molecules absorbed on it. Therefore, the reutility and stability of the magnetic Fe_3O_4/Bi_2S_3 MSs were examined through the repeated experiments based on the two different experimental procedures: (1) only adsorption in dark and (2) simultaneous adsorption and photocatalytic regeneration in one step for cycling under simulated solar light irradiation. Fig. 8 shows the successive

cycles of two different experimental procedures. The adsorption capacities for Fe_3O_4/Bi_2S_3 MSs decreased noticeably during the repeated adsorption operations. An obvious decrease from 91.60% to 40.3% in the removal efficiency was observed when the magnetic Fe_3O_4/Bi_2S_3 MSs were reused as adsorbent for the first cycle (Fig. 8 curve a). After the successive fifth cycles, the removal efficiency was only 25.3% by only adsorption in dark. The decreased efficiency after five cycles may be due to the decreased surface active sites. Interestingly, when the adsorption and photocatalytic regeneration were simultaneously performed during the repeated experiments under simulated solar light irradiation, the recyclability of the magnetic Fe_3O_4/Bi_2S_3 MSs can be improved efficiently compared with the reuse of Bi_2S_3 MSs. As shown in Fig. 8 curve b, the magnetic Fe_3O_4/Bi_2S_3 MSs exhibited good stability and maintained high removal efficiency in successive five cycles under simulated solar light irradiation. What's more, the magnetic Fe_3O_4/Bi_2S_3 MSs did not show a clear decrease in photodegradation efficiency after Fe_3O_4/Bi_2S_3 MSs were used for fifth time recycles for the decolorization of CR under simulated light irradiation. The enhanced decolorization of CR solution by Fe_3O_4/Bi_2S_3 MSs resulted from two main reasons. Firstly, Fe_3O_4/Bi_2S_3 MSs can concentrate the targeted CR dye on the surface of water-treatment materials from the diluted water to promote the CR transfer process. Secondly, CR adsorbed on the surface of Fe_3O_4/Bi_2S_3 MSs can be photocatalytically oxidized and the adsorbent can be regenerated and reused in further cycles [27]. Several studies have shown that CR moleculars can be photodecolorized by appropriated photocatalysts under light irradiation [9,58]. Bi_2S_3 with a typical narrow band gap can be used to photodegrade organic pollutant since Fe_3O_4/Bi_2S_3 MSs have a stronger absorption in the visible light area. In addition, the fact that adsorption and photocatalytic regeneration of organic compounds occur continuously in the presence of Fe_3O_4/Bi_2S_3 MSs avoids two independent processes and reduces the actual processing cost. As a result, magnetically recyclable Fe_3O_4/Bi_2S_3 MSs could be regenerated via the

Table 3
Kinetic parameters of CR adsorption onto Bi_2S_3 MSs and Fe_3O_4/Bi_2S_3 MSs.

Adsorbents	Con. (mg g^{-1})	$q_{e,exp}$ (mg g^{-1})	Lagergren-first-order model			Pseudo-second-order kinetic model			Intraparticle diffusion model		
			$q_{e,exp}$ (mg g^{-1})	k_1 (min^{-1})	R^2	$q_{e,exp}$ (mg g^{-1})	k_2 (mg g^{-1} min^{-1})	R^2	k_i (mg g^{-1} min$^{-1/2}$)	c (mg g^{-1})	R^2
Bi_2S_3	10	10.08	5.03	0.134	0.935	10.13	0.292	1.000	0.986	3.39	0.634
	30	23.34	14.42	0.031	0.976	24.10	0.006	0.998	1.268	8.92	0.707
Fe_3O_4/Bi_2S_3	10	9.81	2.10	0.097	0.760	9.84	1.321	1.000	0.778	4.15	0.531
	30	27.98	9.31	0.024	0.905	28.26	0.010	0.999	1.160	14.33	0.524
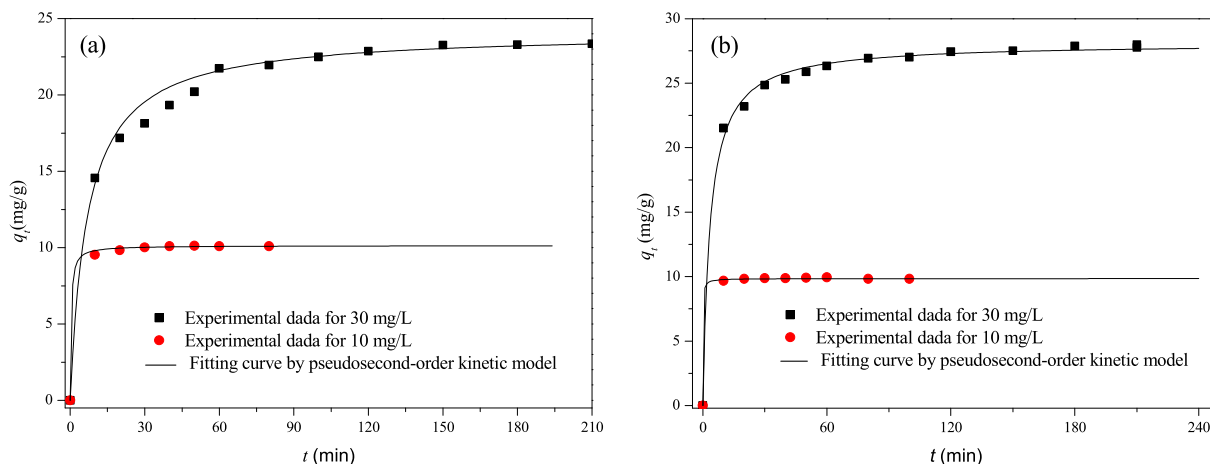
Fig. 7. Fitting of pseudosecond-order kinetics for CR adsorption on Bi_2S_3 MSs (a) and Fe_3O_4/Bi_2S_3 MSs (b). Experimental conditions: initial CR concentration 30 mg L^{-1}; adsorbent dosage 1.0 g L^{-1}
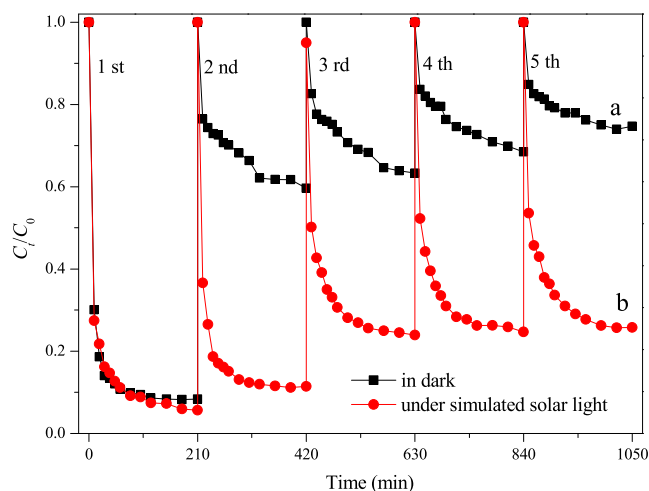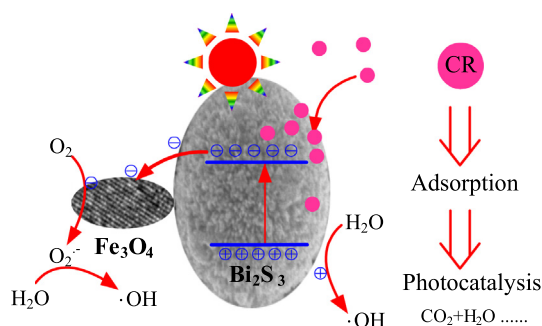

Fig. 8. Recycling test of the magnetic Fe_3O_4/Bi_2S_3 MSs performed in dark (a) and under simulated solar light irradiation (b).

Fig. 9. Mechanism of CR removal on Fe_3O_4/Bi_2S_3 MSs under simulated solar light illumination.

economical, green photocatalytic treatment and maintain higher processing removal efficiency of CR dye by adsorption and photocatalytic regeneration.
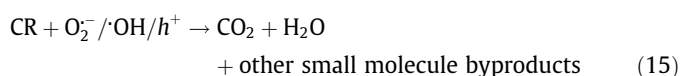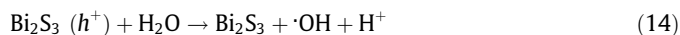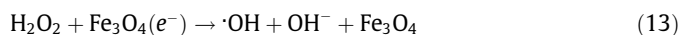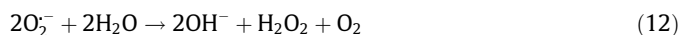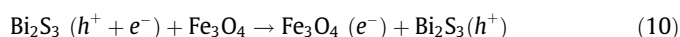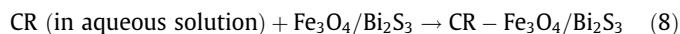
3.6. The possible mechanism of dye removal by Fe_3O_4/Bi_2S_3 MSs

As previous studies mentioned [29,46], the photodegradation of dye pollutants on photocatalyst is mainly driven by a series of reactive species including active holes (h^+), hydroxyl radicals (·OH), and superoxide radicals (O_2^-) generated. Based on the above experimental results and corresponding Refs. [44,46], a possible mechanism of successful CR removal by Fe_3O_4/Bi_2S_3 MSs under simulated solar light irradiation was proposed as follows (Fig. 9). Firstly, CR molecules in aqueous solution were adsorbed fast onto Fe_3O_4/Bi_2S_3 MSs (Eq. (8)) due to the high relative large surface areas and mesoporous channels of magnetic Fe_3O_4/Bi_2S_3. At the same time, electrons (e^-) in the valence band (VB) of Bi_2S_3 in Fe_3O_4/Bi_2S_3 MSs can be photoexcited to its conduction band (CB) under simulated light irradiation, causing the photoproduced holes (h^+) in the VB of Bi_2S_3 simultaneously (Eq. (9)). The CB level of Fe_3O_4 (1 V vs. NHE) is much lower than that of Bi_2S_3 (0.12 V vs. NHE) [22,46], so the photoproduced $Bi_2S_3(e^-)$ may quickly migrate from conduction band of Bi_2S_3 MSs into that of the Fe_3O_4 and the

chance of e^-/h^+ recombination is greatly reduced (Eq. (10)). Following, the migrated e^- reacted with the oxygen molecule (O_2) that dissolved in aqueous solution to yield O_2^- (Eq. (11)) [29], which further react with H_2O and to produce H_2O_2 and ·OH (Eqs. (12) and (13)). The photoinduced holes (h^+) at the VB top of Bi_2S_3 with potential of about 2.07 eV [31], which is more positive than the standard reduction potential of OH$^-$/·OH(1.99 eV), can react with H_2O to produce ·OH radicals (Eq. (14)). At last, all the produced active species including ·OH, e^-/h^+ and O_2^- can attacked the N=N bonds of CR molecules adsorbed on Fe_3O_4/Bi_2S_3 MSs and further oxidize the broken CR molecules into CO_2, H_2O and other small molecule byproducts (Eq. (15)) [29].

$$CR \text{ (in aqueous solution)} + Fe_3O_4/Bi_2S_3 \rightarrow CR - Fe_3O_4/Bi_2S_3 \quad (8)$$

$$Bi_2S_3 + h\nu \rightarrow Bi_2S_3 \ (h^+ + e^-) \quad (9)$$

$$Bi_2S_3 \ (h^+ + e^-) + Fe_3O_4 \rightarrow Fe_3O_4 \ (e^-) + Bi_2S_3(h^+) \quad (10)$$

$$Fe_3O_4 \ (e^-) + O_2 \rightarrow Fe_3O_4 + O_2^- \quad (11)$$

$$2O_2^- + 2H_2O \rightarrow 2OH^- + H_2O_2 + O_2 \quad (12)$$

$$H_2O_2 + Fe_3O_4(e^-) \rightarrow \cdot OH + OH^- + Fe_3O_4 \quad (13)$$

$$Bi_2S_3 \ (h^+) + H_2O \rightarrow Bi_2S_3 + \cdot OH + H^+ \quad (14)$$

$$CR + O_2^-/\cdot OH/h^+ \rightarrow CO_2 + H_2O$$
$$+ \text{ other small molecule byproducts} \quad (15)$$

4. Conclusions

In summary, magnetically recyclable Fe_3O_4/Bi_2S_3 MSs combining the highly effective adsorption and green photocatalytic regeneration were prepared by a facile hydrothermal method. The as-obtained Fe_3O_4/Bi_2S_3 MSs possessed a relative high surface area, low coercivity value and remanent magnetization value. The Fe_3O_4/Bi_2S_3 MSs can be easily and economically separated, regenerated and re-dispersed in aqueous solution, which is desirable for practical application. The equilibrium and kinetics of adsorption process followed the Langmuir isotherm model and pseudo-second-order kinetic for CR adsorption on Fe_3O_4/Bi_2S_3 MSs, respectively. The maximum adsorption capacity of CR for Fe_3O_4/Bi_2S_3 MSs as 92.24 mg g^{-1} was achieved by Langmuir isotherm model, while only 66.28 mg g^{-1} was found for Bi_2S_3 MSs. Fe_3O_4/Bi_2S_3 MSs also show excellent stability and reusability for effective removal of Congo red dye by simultaneous adsorption and photocatalytic regeneration. As a result, Fe_3O_4/Bi_2S_3 MSs provide effective and conveniently recyclable materials for the environmental remediation and purification of wastewater by providing the facile preparation, easy magnetic separation, high adsorption, and simple regeneration.

Acknowledgments

References

[1] A. Ahmad, S.H. Mohd-Setapar, C.S. Chuong, A. Khatoon, W.A. Wani, R. Kumar, M. Rafatullah, Recent advances in new generation dye removal technologies: novel search for approaches to reprocess wastewater, RSC Adv. 5 (2015) 30801–30818.

[2] D.W. Cho, B.H. Jeon, C.M. Chon, F.W. Schwartz, Y. Jeong, H. Song, Magnetic chitosan composite for adsorption of cationic and anionic dyes in aqueous solution, J. Ind. Eng. Chem. 20 (2014) 3559–3567.

[3] H.Y. Zhu, Y.Q. Fu, R. Jiang, J.H. Jiang, L. Xiao, G.M. Zeng, S.L. Zhao, Y. Wang, Adsorption removal of Congo red onto magnetic cellulose/Fe_3O_4/activated carbon composite: equilibrium, kinetic and thermodynamic studies, Chem. Eng. J. 173 (2011) 494–502.

[4] M. Riera-Torres, C. Gutiérrez-Bouzán, M. Crespi, Combination of coagulation–flocculation and nanofiltration techniques for dye removal and water reuse in textile effluents, Desalination 252 (2010) 53–59.

[5] J. Ferre-Aracil, S.C. Cardona, J. Navarro-Laboulais, Ozonation kinetics of acid red 27 azo dye: a novel methodology based on artificial neural networks for the determination of dynamic kinetic constants in bubble column reactors, Chem. Eng. Commun. 202 (2015) 279–293.

[6] S. Chakma, J.B. Bhasarkar, V.S. Moholkar, Preparation, characterization and application of sonochemically doped Fe^{3+} into ZnO nanoparticles, Int. J. Res. Eng. Technol. 2 (2013) 177–183.

[7] S. Chakma, V.S. Moholkar, Investigation in mechanistic issues of sonocatalysis and sonophotocatalysis using pure and doped photocatalysts, Ultrason. Sonochem. 22 (2015) 287–299.

[8] Z.T. Hu, J. Liu, X. Yan, W.D. Oh, T.T. Lim, Low-temperature synthesis of graphene/$Bi_2Fe_4O_9$ composite for synergistic adsorption–photocatalytic degradation of hydrophobic pollutant under solar irradiation, Chem. Eng. J. 262 (2015) 1022–1032.

[9] R. Jiang, J. Yao, H. Zhu, Y. Fu, Y. Guan, L. Xiao, G. Zeng, Effective decolorization of Congo red in aqueous solution by adsorption and photocatalysis using novel magnetic alginate/γ–Fe_2O_3/CdS nanocomposite, Desalinat. Water Treat. 52 (2014) 238–247.

[10] H.Y. Jing, T. Wen, C.M. Fan, G.Q. Gao, S.L. Zhong, A.W. Xu, Efficient adsorption/photodegradation of organic pollutants from aqueous systems using Cu_2O nanocrystals as a novel integrated photocatalytic adsorbent, J. Mater. Chem. A 2 (2014) 14563–14570.

[11] M.L. Yola, T. Eren, N. Atar, S. Wang, Adsorptive and photocatalytic removal of reactive dyes by silver nanoparticle–colemanite ore waste, Chem. Eng. J. 242 (2014) 333–340.

[12] L. Zhang, H. Li, Y. Liu, Z. Tian, B. Yang, Z. Sun, S. Yan, Adsorption–photocatalytic degradation of methyl orange over a facile one–step hydrothermally

[13] synthesized TiO$_2$/ZnO–NH$_2$–RGO nanocomposite, RSC Adv. 4 (2014) 48703–48711.

[13] H.Y. Zhu, R. Jiang, S.H. Huang, J. Yao, F.Q. Fu, J.B. Li, Novel magnetic NiFe$_2$O$_4$/multi–walled carbon nanotubes hybrids: facile synthesis, characterization, and application to the treatment of dyeing wastewater, Ceram. Int. 41 (2015) 11625–11631.

[14] X. Gao, H.B. Wu, L. Zheng, Y. Zhong, Y. Hu, X.W.D. Lou, Formation of mesoporous heterostructured BiVO$_4$/Bi$_2$S$_3$ hollow discoids with enhanced photoactivity, Angew. Chem. 126 (2014) 6027–6031.

[15] T. Wu, X.G. Zhou, H. Zhang, X.H. Zhong, Bi$_2$S$_3$ nanostructures: a new photocatalyst, Nano Res. 3 (2010) 379–386.

[16] Z. Zhang, W. Wang, L. Wang, S. Sun, Enhancement of visible–light photocatalysis by coupling with narrow–band–gap semiconductor: a case study on Bi$_2$S$_3$/Bi$_2$WO$_6$, ACS Appl. Mater. Interfaces 4 (2012) 593–597.

[17] H. Bao, X. Cui, C.M. Li, Y. Gan, J. Zhang, J. Guo, Photoswitchable semiconductor bismuth sulfide [Bi$_2$S$_3$] nanowires and their self-supported nanowire arrays, J. Phys. Chem. C 111 (2007) 12279–12283.

[18] J.F. Cabrita, V.C. Ferreira, O.C. Monteiro, Titanate nanofibers sensitized with nanocrystalline Bi$_2$S$_3$ as new electrocatalytic materials for ascorbic acid sensor applications, Electrochim. Acta 135 (2014) 121–127.

[19] G. Chen, Y. Yu, K. Zheng, T. Ding, W. Wang, Y. Jiang, Q. Yang, Fabrication of ultrathin Bi$_2$S$_3$ nanosheets for high–performance, flexible, visible–NIR photodetectors, Small 11 (2015) 2848–2855.

[20] G. Konstantatos, L. Levina, J. Tang, E.H. Sargent, Sensitive solution–processed Bi$_2$S$_3$ nanocrystalline photodetectors, Nano Lett. 8 (2008) 4002–4006.

[21] H. Li, J. Yang, J. Zhang, M. Zhou, Facile synthesis of hierarchical Bi$_2$S$_3$ nanostructures for photodetector and gas sensor, RSC Adv. 2 (2012) 6258–6261.

[22] X. Rong, F. Qiu, J. Yan, H. Zhao, X. Zhu, D. Yang, Coupling with a narrow–band–gap semiconductor for enhancement of visible–light photocatalytic activity: preparation of Bi$_2$S$_3$/g–C$_3$N$_4$ and application for degradation of RhB, RSC Adv. 25 (2015) 24944–24952.

[23] A. Sarkar, A.B. Ghosh, N. Saha, A.K. Dutta, D.N. Srivastava, P. Paul, B. Adhikary, Enhanced photocatalytic activity of Eu–doped Bi$_2$S$_3$ nanoflowers for degradation of organic pollutants under visible light illumination, Catal. Sci. Technol. 5 (2015) 4055–4063.

[24] B. Weng, X. Zhang, N. Zhang, Z.R. Tang, Y.J. Xu, Two–dimensional MoS$_2$ nanosheet–coated Bi$_2$S$_3$ discoids: synthesis, formation mechanism, and photocatalytic application, Langmuir 31 (2015) 4314–4322.

[25] M. Aresti, M. Saba, R. Piras, D. Marongiu, G. Mula, F. Quochi, A. Mura, C. Cannas, M. Mureddu, A. Ardu, G. Ennas, V. Calzia, A. Mattoni, A. Musinu, G. Bongiovanni, Colloidal Bi$_2$S$_3$ nanocrystals: quantum size effects and midgap states, Adv. Funct. Mater. 24 (2014) 3341–3350.

[26] Y. Bessekhouad, M. Mohammedi, M. Trari, Hydrogen photoproduction from hydrogen sulfide on Bi$_2$S$_3$ catalyst, Sol. Energy Mater. Sol. Cells 73 (2002) 339–350.

[27] R. Albuquerque, M.C. Neves, M.H. Mendonca, T. Trindade, O.C. Monteiro, Adsorption and catalytic properties of SiO$_2$/Bi$_2$S$_3$ nanocomposites on the methylene blue photodecolorization process, Colloids Surf. A 328 (2008) 107–113.

[28] J. Zhou, G. Tian, Y. Chen, Y. Shi, C. Tian, K. Pan, H. Fu, Growth rate controlled synthesis of hierarchical Bi$_2$S$_3$/In$_2$S$_3$ core/shell microspheres with enhanced photocatalytic activity, Sci. Rep. 4 (2014) 4027–4036.

[29] J. Cao, B. Xu, H. Lin, B. Luo, S. Chen, Novel Bi$_2$S$_3$–sensitized BiOCl with highly visible light photocatalytic activity for the removal of rhodamine B, Catal. Commun. 26 (2012) 204–208.

[30] Z.Q. Liu, W.Y. Huang, Y.M. Zhang, Y.X. Tong, Facile hydrothermal synthesis of Bi$_2$S$_3$ spheres and CuS/Bi$_2$S$_3$ composites nanostructures with enhanced visible–light photocatalytic performances, Cryst. Eng. Comm. 14 (2012) 8261–8267.

[31] X. Liu, W. Wang, Y. Liu, B. Huang, Y. Dai, X. Qin, X. Zhang, In situ synthesis of Bi$_2$S$_3$/Bi$_2$SiO$_5$ heterojunction photocatalysts with enhanced visible light photocatalytic activity, RSC Adv. 5 (2015) 55957–55963.

[32] C.T. Yavuz, J.T. Mayo, W.W. Yu, A. Prakash, J.C. Falkner, S. Yean, L. Cong, H.J. Shipley, A. Kan, M. Tomson, D. Natelson, V.L. Colvin, Low-field magnetic separation of monodisperse Fe$_3$O$_4$ nanocrystals, Science 314 (2006) 964–967.

[33] J.G. McEvoy, Z. Zhang, Synthesis and characterization of magnetically separable Ag/AgCl–magnetic activated carbon composites for visible light induced photocatalytic detoxification and disinfection, Appl. Catal., B 160–161 (2014) 267–278.

[34] M.A. Salam, R.M. El-Shishtawy, A.Y. Obaid, Synthesis of magnetic multi-walled carbon nanotubes/magnetite/ chitin magnetic nanocomposite for the removal of Rose Bengal from real and model solution, J. Ind. Eng. Chem. 20 (2014) 3559–3567.

[35] H.Y. Zhu, R. Jiang, L. Xiao, W. Li, A novel magnetically separable γ–Fe$_2$O$_3$/crosslinked chitosan adsorbent: preparation, characterization and adsorption application for removal of hazardous azo dye, J. Hazard. Mater. 179 (2010) 251–257.

[36] T. Harifi, M. Montazer, A novel magnetic reusable nanocomposite with enhanced photocatalytic activities for dye degradation, Sep. Purif. Technol. 134 (2014) 210–219.

[37] Z. He, T. Hong, J. Chen, S. Song, A magnetic TiO$_2$ photocatalyst doped with iodine for organic pollutant degradation, Sep. Purif. Technol. 96 (2012) 50–57.

[38] P. Zhang, Z. Mo, L. Han, X. Zhu, B. Wang, C. Zhang, Preparation and photocatalytic performance of magnetic TiO$_2$/montmorillonite/Fe$_3$O$_4$ nanocomposites, Ind. Eng. Chem. Res. 53 (2014) 8057–8061.

[39] R. Jiang, H.Y. Zhu, J.B. Li, F.Q. Fu, J. Yao, S.T. Jiang, G.M. Zeng, Fabrication of novel magnetically separable BiOBr/CoFe$_2$O$_4$ microspheres and its application in the efficient removal of dye from aqueous phase by an environment-friendly and economical approach, Appl. Surf. Sci. 364 (2015) 604–612.

[40] X. Li, C. Niu, D. Huang, X. Wang, X. Zhang, G. Zeng, Q. Niu, Preparation of magnetically separable Fe$_3$O$_4$/BiOI nanocomposites and its visible photocatalytic activity, Appl. Surf. Sci. 286 (2013) 40–46.

[41] Y.F. Zhang, L.G. Qiu, Y.P. Yuan, Y.J. Zhu, X. Jiang, J.D. Xiao, Magnetic Fe$_3$O$_4$@C/Cu and Fe$_3$O$_4$@CuO core–shell composites constructed from MOF–based materials and their photocatalytic properties under visible light, Appl. Catal., B 144 (2014) 863–869.

[42] M. Farrokhi, S.C. Hosseini, J.K. Yang, M. Shirzad-Siboni, Application of ZnO–Fe$_3$O$_4$ nanocomposite on the removal of azo dye from aqueous solutions: kinetics and equilibrium studies, Water Air Soil Pollut. 225 (2014) 2113–2124.

[43] Y.R. Yao, W.Z. Huang, H. Zhou, H.Y. Yin, Y.F. Zheng, X.C. Song, A novel Fe$_3$O$_4$@SiO$_2$@BiOBr photocatalyst with highly active visible light photocatalytic properties, Mater. Chem. Phys. 148 (2014) 896–902.

[44] C. Karunakaran, P. Vinayagamoorthy, J. Jayabharath, Nonquenching of charge carriers by Fe$_3$O$_4$ core in Fe$_3$O$_4$/ZnO nanosheet photocatalyst, Langmuir 30 (2014) 15031–15039.

[45] X. Bian, K. Hong, X. Ge, R. Song, L. Liu, M. Xu, Functional hierarchical nanocomposites based on ZnO nanowire and magnetic nanoparticle as highly active recyclable photocatalysts, J. Phys. Chem. C119 (2015) 1700–1705.

[46] Y. Cao, C. Li, J. Li, Q. Li, J. Yang, Magnetically separable Fe$_3$O$_4$/AgBr hybrid materials: highly efficient photocatalytic activity and good stability, Nanoscale Res. Lett. 10 (2015) 251–256.

[47] J. Chen, S. Qin, G. Song, T. Xiang, F. Xin, X. Yin, Shape–controlled solvothermal synthesis of Bi$_2$S$_3$ for photocatalytic reduction of CO$_2$ to methyl formate in methanol, Dalton Trans. 42 (2013) 15133–15138.

[48] Y. Wang, J. Chen, P. Wang, L. Chen, Y.B. Chen, L.M. Wu, Syntheses, growth mechanism, and optical properties of [001] growing Bi$_2$S$_3$ nanorods, J. Phys. Chem. C 113 (2009) 16009–16014.

[49] D.K. Ma, M.L. Guan, S.S. Liu, Y.Q. Zhang, C.W. Zhang, Y.X. He, S.M. Huang, Controlled synthesis of olive-shaped Bi$_2$S$_3$/BiVO$_4$ microspheres through a limited chemical conversion route and enhanced visible-light-responding photocatalytic activity, Dalton Trans. 41 (2012) 5581–5586.

[50] Y. Li, F. Wei, Y. Ma, H. Zhang, Z. Gao, L. Dai, G. Qin, Selected–control hydrothermal synthesis and photoresponse properties of Bi$_2$S$_3$ micro/nanocrystals, Cryst. Eng. Comm. 15 (2013) 6611–6616.

[51] S. Si, C. Li, X. Wang, D. Yu, Q. Peng, Y. Li, Magnetic monodisperse Fe$_3$O$_4$ nanoparticles, Cryst. Growth Des. 5 (2005) 391–393.

[52] C. Wang, Y. Zhou, M. Ge, X. Xu, Z. Zhang, J.Z. Jiang, Large-scale synthesis of SnO$_2$ nanosheets with high lithium storage capacity, J. Am. Chem. Soc. 132 (2010) 46–47.

[53] L. Wang, J. Li, Y. Wang, L. Zhao, Preparation of nanocrystalline Fe$_{3−x}$La$_x$O$_4$ ferrite and their adsorption capability for Congo red, J. Hazard. Mater. 196 (2011) 342–349.

[54] R. Rahimi, H. Kerdari, M. Rabbani, M. Shafiee, Synthesis, characterization and adsorbing properties of hollow Zn-Fe$_2$O$_4$ nanospheres on removal of Congo red from aqueous solution, Desalination 280 (2011) 412–418.

[55] L. Lian, L. Guo, C. Guo, Adsorption of Congo red from aqueous solutions onto Ca-bentonite, J. Hazard. Mater. 161 (2009) 126–131.

[56] H. Zhu, M. Zhang, Y. Liu, L. Zhang, R. Han, Study of Congo red adsorption onto chitosan coated magnetic iron oxide in batch mode, Desalinat. Water Treat. 37 (2012) 46–54.

[57] C. Namasivayam, D. Kavitha, Removal of Congo Red from water by adsorption onto activated carbon prepared from coir pith, an agricultural solid waste, Dyes Pigm. 54 (2002) 47–58.

[58] H. Zhu, R. Jiang, L. Xiao, Y. Chang, Y. Guan, X. Li, G. Zeng, Photocatalytic decolorization and degradation of Congo Red on innovative crosslinked chitosan/nano-CdS composite catalyst under visible light irradiation, J. Hazard. Mater. 169 (2009) 933–940.